Improved Palm Oil Mill Effluent Degradation by Fe^{2+}/Fe^{3+} Ion Exchanger Mediator

Mohd Hafiz Md Ali[1], Mohd Afiq Mohd Fauzi[2*], Mohammad Noor Jalil[1,3], Zainiharyati Mohd Zain[1,3], Tay Chia Chay[1], Hamizah Mohd Zaki[1]

[1]*Faculty of Applied Sciences, Universiti Teknologi MARA, 40450 Shah Alam, Selangor, Malaysia*
[2]*Civil Engineering Studies, College of Engineering, Universiti Teknologi MARA, 94300 Kota Samarahan, Sarawak, Malaysia*
[3]*Electrochemical Material and Sensor (EMaS) Research Group, Faculty of Applied Sciences, Universiti Teknologi MARA, 40450 Shah Alam, Selangor, Malaysia*

ARTICLE INFO

ABSTRACT

This present study investigates the efficiency of using ion exchanger Fe^{2+}/Fe^{3+} mediator for the degradation of Palm Oil Mill Effluent (POME). The ion exchanger of Fe^{2+}/Fe^{3+} mediator enhanced the redox reaction in liquid POME degradation. Comprehensive analysis on POME before and after degradation by 0.005 M $FeCl_3$ was conducted by several characterisation techniques, including cyclic voltammetry (CV), Ultraviolet-visible (UV-Vis) spectroscopy, Attenuated Total Reflectance-Fourier Transform Infrared spectroscopy (ATR-FTIR) Analysis, X-ray diffraction (XRD), and Brunauer-Emmett-Teller (BET) analysis. The CV analysis provided a better understanding on the oxidation and reduction reaction during the degradation of liquid POME. The identification of chemical bonds and functional groups was carried out by using the ATR-FTIR analysis. The type of crystal or amorphous patterns identified by XRD and surface area measurements were done by using the BET analysis. The findings revealed that the existence of ion exchanger Fe^{2+}/Fe^{3+} mediator performed redox reaction by CV and the peak current density of oxidation (Ipa) showed similar results for fresh liquid POME and liquid POME+0.005 M $FeCl_3$, that is $1.34 \times 10^{-1}\mu A\ cm^{-2}$. Meanwhile, the peak current density of reduction (Ipc) for both samples were $-1.33 \times 10^{2}\ \mu A\ cm^{-2}$ and -5.89×10^{1} $\mu A\ cm^{-2}$, respectively. The specific capacitance, C are 125.08 C and 157.71 C for both samples. Spectrometry analysis by UV-Vis

[2*] Corresponding author. *E-mail address*: mohdafiq3474@uitm.edu.my
https://doi.org/10.24191/jsst.v5i1.90

spectrometry showed a significant absorbance reduction and chemical shifting when 0.005 M $FeCl_3$ was added to liquid POME. By using the ATR-FTIR analysis, it was revealed that the chemical bonds changed on dried solid POME after degradation with the addition of 0.005 M $FeCl_3$. Amorphous diffractogram patterns were identified for both samples by XRD analysis. An increase in surface area from 0.94 $m^2\,g^{-1}$ to 18.55 $m^2\,g^{-1}$ was also revealed from the BET analysis. This research contributes to the knowledge on the role of ion exchangers Fe^{2+}/Fe^{3+} mediator, providing a foundation for effective liquid POME treatment.

1   INTRODUCTION

Palm Oil Mill Effluent (POME) is highly concentrated wastewater generated during the palm oil production process. It is crucial to treat POME for sustainable palm oil production since it has substantial organic content and the potential of harming the environment[1–4]. The use of Fe^{2+}/Fe^{3+} ion exchangers mediators in POME degradation proven to be an effective application. The existence of these ions improves the redox reactions, and hence, the improvement in the effluent quality by facilitating the degradation of contaminants in liquid POME. The degradation reaction and rate of biomass like POME are affected by factors, such as temperature, pH, and concentration[5–7]. A study conducted by Abeish et al.[8] showed that the efficiency of heterogeneous photocatalytic degradation processes can be enhanced by including both Fe^{2+} and Fe^{3+} as ion exchangers. The iron ions, which are mediators in oxidation and reduction reactions, influence the properties and chemical behaviour of substances in liquid POME. The ion mediator that uses the Fe^{2+}/Fe^{3+} exchanger is also involved in various catalytic processes. The transfer of Fe ions between different oxidation states is essential[9,10]. In specific reactions such as the Fenton reaction, the conversion of Fe^{3+} to Fe^{2+} plays a crucial role. This process enables the Fe^{2+} ion to be part of the generation of hydroxyl radicals[11]. The importance of the Fe^{2+}/Fe^{3+} ratio is shown by the enhanced catalytic efficiency of Cu, Mg, and Fe in layered double hydroxides with specific Fe^{2+}/Fe^{3+} ions ratios[12]. In addition, the catalytic activity can be influenced by the variations in the electronic structure of ion Fe in catalysts, which is dependent on their oxidation states[13]. In this study, 0.005 M $FeCl_3$ is ideal for the process of degradation by Fe^{2+}/Fe^{3+} ion exchanger mediator set at room temperature. Characterisation techniques such as ultraviolet-visible (UV-Vis) and Attenuated Total Reflectance-Fourier Transform Infrared spectroscopy (ATR-FTIR), Cyclic Voltammetry (CV), X-ray Diffraction (XRD), and Brunauer-Emmett-Teller (BET) were applied. This study offers valuable insights into the efficacy of Fe^{2+}/Fe^{3+} ion exchangers for the chemical degradation of organic compounds in liquid POME. This method of using Fe^{2+}/Fe^{3+} ion exchanger mediator is a better strategy to enhance the effectiveness of liquid POME degradation.

2   EXPERIMENTAL

2.1   Chemical and materials

Iron (III) chloride hexahydrate ($FeCl_3 \cdot 6H_2O$), and Crystal AR were obtained from HmbG® Chemical, Germany. Hydrochloric Acid (HCl), 37%, Sigma-Aldrich, USA, and 100 mL of liquid Palm Oil Mill Effluent (POME) were used for the analysis. All chemicals were used as received unless otherwise stated.

2.2   Methodology

The effect of degradation and synthesis organic reaction of POME were characterized by using different techniques to emphasise the changes in the Fe^{2+}/Fe^{3+} ion exchange mediator. The main goal of this study is to analyse the effect of liquid POME utilised for degradation reaction with 0.005 M $FeCl_3$ as a catalyst set at room temperature. 5 L of liquid POME were sampled at Sime Darby Research Centre, Pulau Carey, Selangor, Malaysia. After sampling, the fresh liquid POME was kept at 4 ºC in a chiller before analysis.

Cyclic voltammetry (CV) for Fe^{2+}/Fe^{3+} mediated ion exchange analysis

This analysis evaluates the effectiveness and capability of Fe^{2+}/Fe^{3+} ion exchangers by adding 0.005 M $FeCl_3$ to the liquid POME. It employs the Fe^{2+}/Fe^{3+} ion exchange in liquid POME to evaluate its ability to perform redox reactions and enhance the degradation of liquid POME. The CV analysis was carried out by using a portable instrument, µStat 300 Biopotentiostat (STAT300 Metrohm). The setup for Cyclic Voltammetry (CV) consisted of a three-electrode system, including a Glassy Carbon Electrode (GCE), a silver/silver chloride (Ag/AgCl) as a reference electrode, and Platinum (Pt) as a counter electrode. The potential window was set up from −1.0 to 1.0 V, with a static scan rate of 0.05 V s^{-1} at room temperature.

UV-visible spectroscopy analysis

This study characterises the degradation and synthesis of organic compounds in liquid POME mediated by Fe^{2+}/Fe^{3+} ion exchangers under UV light. The behaviour of absorption and transmission was then evaluated. The instrument used was a double-beam UV-Vis spectrophotometer (PerkinElmer, Lambda 35). It is important to reveal the information on the electronic transitions and oxidation states of the ions. Prior to the analysis, 3.5 mL of the liquid POME sample was obtained. Then, 0.005 M $FeCl_3$ was added to ten percent of the total volume of liquid POME and vortexed to homogenise the sample. The analysis to measure the absorbance (a.u.) was set within the 200 to 600 nm wavelength range. Each sample was performed in triplicate. This UV-Vis analysis, one of the non-destructive techniques, offers studies on various materials, including organic compounds and metal ions[14]. The standard guideline for this analysis is in line with the Standard Practices for General Techniques of Ultraviolet-Visible Quantitative Analysis (ASTM E1169-16).

ATR-FTIR analysis

This experimental study using ATR-FTIR analysis aims to characterize the chemical composition and identify chemical bonds found in the samples by focusing on the vibration of molecules. The investigation was conducted by using the PerkinElmer 1600 Series FTIR instrument. Dried solid POME was prepared by placing 100 mL of liquid POME in a porcelain crucible and drying it at 104 ± 1ºC for one hour in an oven. Subsequently, it was allowed to cool in a desiccator and weighed. The standard used was the Standard Methods Committee of the American Public Health Association APHA-2540 solids- Standard Methods for the Examination of Water and Wastewater. This analysis required 3 g of material. Before the analysis, the wavelength range was set from 4,000 nm to 1,000 nm, with the scan number applied 20 times. When the parameters were set, the sample was placed in close contact with the ATR crystal. This analysis followed closely the ASTM E168, (amendment) E1252 Fourier Transform Infrared Spectrometry standard.

X-ray diffraction (XRD) analysis

This analytical technique uses diffraction to measure crystallinity by quantifying the scattering of X-rays. It is used to determine the phase composition and purity of samples. The analysis was conducted by using an XRD instrument - PANalytical X'pert Pro model DY25. The instrument was equipped with a Cu Kα anode and performed at a voltage of 40 kV throughout the analysis. Before performing the analysis, 2 g of each dried solid POME, dried solid POME+$FeCl_3$, and catalyst $FeCl_3$ were measured and placed on the sample holders. All the samples of dried solids were prepared in a similar manner using ATR-FTIR analysis. As a standard guideline for analysis, the Standard Guide for Forensic Analysis of Geological Material by Powder X-Ray Diffraction ASTM E3294-22 was observed.

BET porous analysis

The Brunauer-Emmett-Teller (BET) method is used to measure the specific surface area of a substance by estimating the quantity of gas absorbed onto its surface. The analysis began with weighing of 0.12 g sample, which must undergo a degassing process performed by the Micromeritics Smart Prep Programmable Degas System. Then, a separate instrument from Micromeritics ASAP 2060 was used for porous analysis. The main procedures involved were degassing, dehydrating, and purifying, which were necessary for all the samples. This was then followed by exposing the sample to nitrogen gas at room

temperature for porous analysis. The temperature program was set between 150 ºC and 300 ºC. The output of this analytical data was utilized to examine the adsorption and desorption processes that can be used to determine the specific surface area per unit mass. The BET analysis is capable of dealing with different pressures and providing data on the distribution of pore sizes and the total volume of pores in a material. The Standard Test Method for Carbon Black-total and External Surface Area by Nitrogen Adsorption, ASTM D6556-21 was used as a guideline for this analysis.

3   RESULTS AND DISCUSSION

3.1   Cyclic voltammetry (CV) analysis

Fig. 1 (a) and (b) show the cyclic voltammetry (CV) curves which are also known as voltammograms. This analysis involves a redox reaction to assess the current response of electroactive species to a sweeping potential. There are two sets of voltammograms (a) and (b), which are (a) Distilled water and 0.005 M $FeCl_3$ and (b) fresh liquid POME and liquid POME+$FeCl_3$. The voltammograms display the electrochemical properties through oxidation and reduction reactions, which are known as redox reactions. They also show the value of current peak density for both oxidation (Ipa) and reduction (Ipc). Fig. 1 (a) displays the CV analysis for distilled water showing the same value for both Ipa and Ipc, that is, 0.94×10^0 µA cm^{-2} and -0.94×10^0 µA cm^{-2}. However, the negative (−) symbol represents reduction reaction to current response. The Ipa and Ipc values for 0.005 M $FeCl_3$ are 1.82×100 µA cm^{-2} and -8.82×100 µA cm^{-2} respectively while the capacitance (C) values for distilled water and 0.005 M $FeCl_3$ are 8.80 C and 1.84 C respectively. This significant relationship between CV and specific capacitance (C) lies in its ability to reveal the mass of active material, Q(C), which is used to describe the energy charge during charge transfer in Fe^{2+}/Fe^{3+} ion exchange mediator through the redox reaction[15].

Fig. 1 (b) shows two voltammograms for liquid POME+$FeCl_3$, indicating lower peak currents at reduction, Ipc (-5.89×10^1 µA cm^{-2}) compared to fresh liquid POME, which has higher Ipc (-1.33×10^2 µA cm^{-2}). This proves that adding 10% of 0.005 M $FeCl_3$ indeed enhanced the redox reaction[16]. The addition of 0.005 M $FeCl_3$ affected the kinetics of the electrochemical reactions. The difference between the forward and backward scans is known as hysteresis, and it represents the area under the voltammograms. When comparing the area under the voltammograms in each sample, it reveals that the fresh liquid POME+$FeCl_3$ is broader than the fresh liquid POME voltammogram. The broad area under each voltammogram indicates the specific capacitance (C) of the sample. When 0.005 M $FeCl_3$ is added to the liquid POME, an increase in the charge transfer species of the electrochemical reaction resulted. This specific capacitance (C) indicates the mass of active material charge measured during the CV analysis[17].

Table 1 displays the data from the CV analysis, showing the response of current values based on the oxidation and reduction reaction. The tabulated data extracted from the peaks on voltammograms represent both anodic peak current density (Ipa) and cathodic peak current density (Ipc). Noticeably, the similar Ipa value (1.34×10^{-1}) of both samples indicates that they display the same behaviour in anodic reactions during this oxidation reaction. In contrast, there are contradictory observations which reveal a difference in the Ipc value, with liquid POME exhibiting a higher current value, µA cm^{-2} (-1.33×10^2), compared to liquid POME+0.005 M $FeCl_3$ (-5.89×10^{-1}). This is caused by the presence of 0.005 M $FeCl_3$, which has stronger influence on the cathodic reaction. The negative (−) sign indicates the current response for the reduction reaction in redox reaction. This CV analysis shows a reversible reaction of the Fe^{2+}/Fe^{3+} ion exchanger mediator and represents the redox reaction behaviour. The specific capacitance value reveals that the catalyst (0.005 M $FeCl_3$) boosted the specific capacitance (C) from 125.08 C to 157.71 C, showing an improvement in the capacitance performance.

(a)

(b)
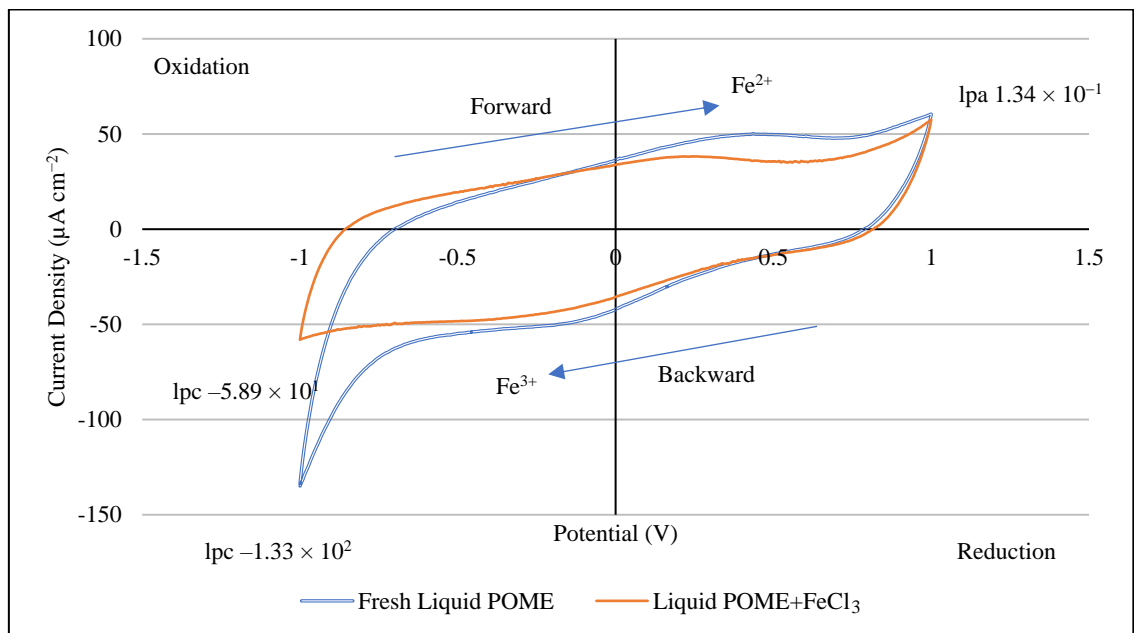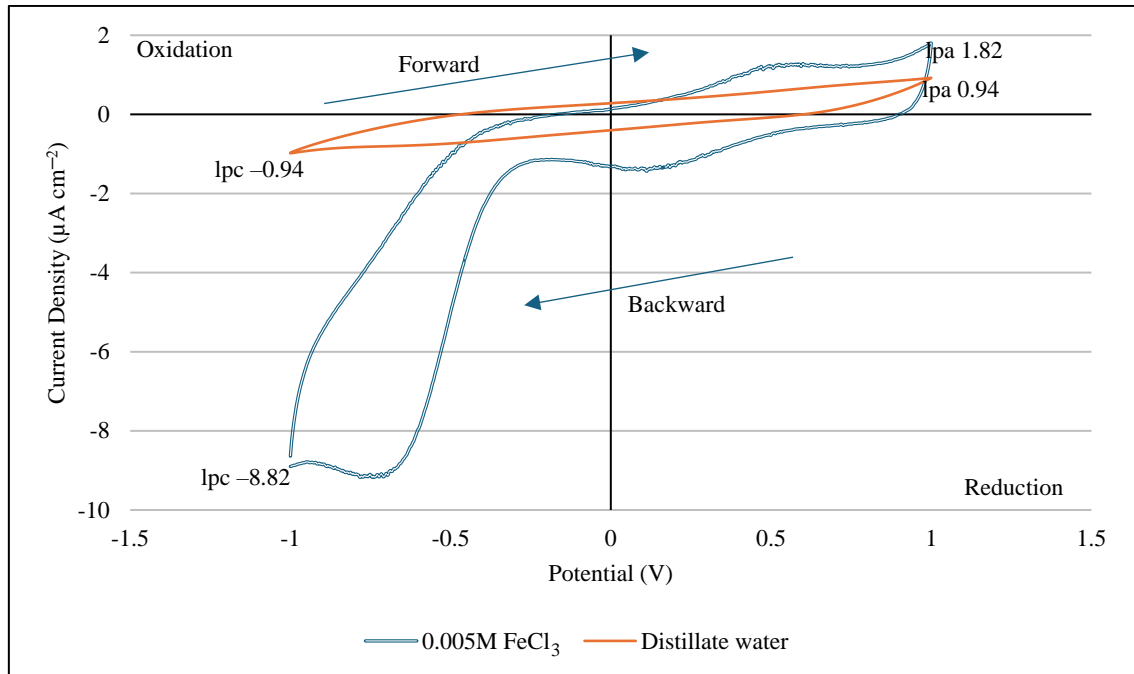
Fig. 1. Voltammograms of CV analysis of (a) Distilled water and 0.005 M FeCl$_3$; (b) Fresh liquid POME, and liquid POME+0.005 M FeCl$_3$.

Table 1. Voltammogram Data from CV analysis of Fresh liquid POME and liquid POME+0.005 M FeCl$_3$

Sample	Anodic peak current density, Ipa (Current µA cm^{-2})	Cathodic peak current density, Ipc (Current µA cm^{-2})	Specific Capacitance (C)
Distilled Water	0.94×10^0	-0.94×10^0	1.84
0.005 M FeCl$_3$	1.82×10^0	-8.82×10^0	8.80
Fresh liquid POME	1.34×10^{-1}	-1.33×10^2	125.08
Liquid POME + 0.005 M FeCl$_3$	1.34×10^{-1}	-5.89×10^1	157.71

During oxidation in the system, Fe^{2+} ions lose an electron to become Fe^{3+} ions in an electrochemical process. Oxidation occurs at the anodic peak potential (Ipa), where the current reaches its maximum value for the oxidation reaction[18]. During electron transfer, the Fe^{2+} ion at the surface of the electrode donates an electron to the electrode. This oxidation process is shown in Equation 1.

$$Fe^{2+} \rightarrow Fe^{3+} + e^- \tag{1}$$

During reduction in the system, Fe^{3+} ions gain an electron to change back to Fe^{2+} ions. Reduction happens at the cathodic peak potential (Ipc), where the current reaches its maximum value for the reduction reaction. Equation 2 shows the reduction mechanism (backward scan),

$$Fe^{3+} + e^- \rightarrow Fe^{2+} \tag{2}$$

3.2   UV-Vis analysis

Three different samples were examined in this study which were 0.005 M FeCl$_3$, liquid POME combined with FeCl$_3$, and fresh liquid POME. Fig. 2 depicts a graph of the absorption spectra, with absorbance (a.u) plotted against wavelength (nm). There are three curves displayed with each representing a different sample, that is, a blue line spectrum for 0.005 M FeCl$_3$, a green line spectrum for fresh liquid POME, and a red line spectrum for POME + 0.005 M FeCl$_3$. Each sample unveiled specific properties in its absorption in UV-Vis radiation. This study examines a UV-Vis absorption spectrum from 200 to 600 nm, with the specific wavelengths at 241 nm and 301 nm represented by dashed lines in yellow. The significance of these wavelengths in absorbance activities and optical properties were characterized[19]. At wavelength 241 nm, the blue line spectrum depicted a fresh liquid POME that has a slightly lower peak absorbance value, 3.00 a.u than the spectrum of 0.005 M FeCl$_3$ solution which is 3.129 a.u. Compared to a wavelength at 301 nm, the absorbance slightly contradicted between fresh liquid POME and 0.005 M FeCl$_3$ solution as their respective absorbance values were 2.87 a.u and 2.96 a.u. This indicates that the 0.005 M FeCl$_3$ has an inherent capacity to efficiently absorb radiation within this particular band of wavelengths. The red line spectrum showed that the liquid POME+FeCl$_3$ sample has the lowest absorbance peak.

At wavelengths of 241 nm and 301 nm, the combination of POME with 0.005 M FeCl$_3$ brought about lower absorbance (a.u.) compared to fresh liquid POME and the 0.005 M FeCl$_3$ solution. It is remarkable that all three spectra displayed a comparable pattern and were characterised by a notable increase in absorbance readings. When comparing the three spectra, it is clear that the introduction of 0.005 M FeCl$_3$ to liquid POME causes an increase in absorbance compared to liquid POME+0.005 M FeCl$_3$. This implies that there may be interactions between FeCl$_3$, and the compounds present in fresh liquid POME, which influence their absorbance ability. Table 2 shows the UV-Vis analysis data on 0.005 M FeCl$_3$ solution, fresh liquid POME, and POME with 0.005 M FeCl$_3$.

In addition, there is no substantial wavelength shift in the three samples when the wavelength is 241 nm. This indicates that the fundamental character of the absorbing species remains unaffected. The changes in absorbance are due to alterations in the absorbing species at a wavelength of 301 nm. It is noted that at 301 nm, the changes in absorbance values are more distinct due to the exchange of Fe^{2+}/Fe^{3+} ions in the ion-exchanger mediator. As predicted, at the wavelength of 301 nm, the reduction of Fe^{3+} ions is more dominant compared to the oxidation of Fe^{2+} ions. This is due to the instability of Fe^{2+} ions compared to the more stable Fe^{3+} ions. The addition of 0.005 M FeCl$_3$ to fresh liquid POME enables it to establish a synthesis

reaction with the organic compounds present. This reaction occurs because 0.005 M $FeCl_3$ itself is an ideal Lewis acid to start the organic synthesis process and result in reduced UV absorbance. However, there is a possibility that other compounds present in the fresh liquid POME may absorb light at similar wavelengths as $FeCl_3$, thus, causing interference and making the absorbance readings less accurate[20].
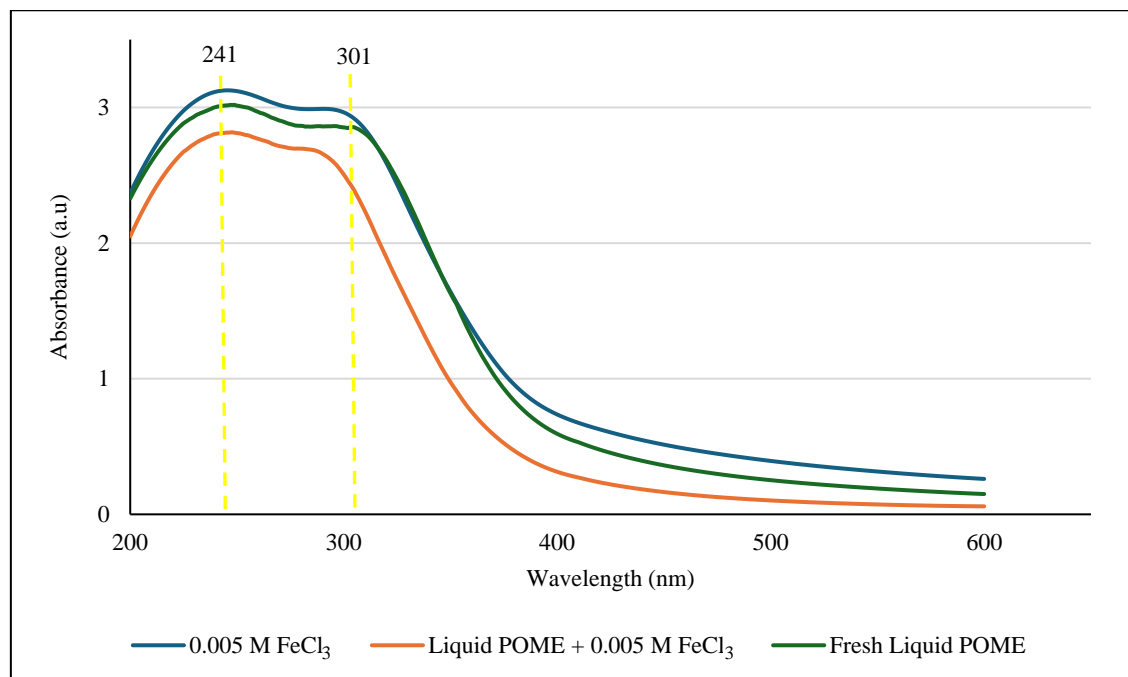
Fig. 2. UV-Vis Spectrum of 0.005 M $FeCl_3$, fresh liquid POME, and liquid POME+0.005 M $FeCl_3$.

Table 2. The absorbance of three samples at wavelengths 241 nm and 301 nm with shifting

Sample	Wavelength, nm		Shifting
	241 Absorbance (a.u)	301 Absorbance (a.u)	
0.005 M $FeCl_3$	3.129	2.96	Absent
Fresh liquid POME	3.00	2.87	Wavelength changed from 301 nm to 306 nm with absorbance changed 2.87 a.u to 2.83 a.u
Liquid POME + 0.005 M $FeCl_3$	2.80	2.47	Wavelength changed from 301 nm to 287 nm with absorbance changed from 2.47 a.u to 2.65 a.u

3.3   Chemical shifting

Complexometric shifts refer to the emergence of new absorption bands in the existing bands probably caused by the existence of metal ions such as Fe^{3+} and ligands. Changes in the concentration of the absorbing species result in variations in absorbance. Generally, it does not change the absorption maximum unless there is aggregation or de-aggregation. The ionization state of the absorbing species might differ, resulting in variations in the absorption spectrum[21]. The absorption peak at around 301 nm in the 0.005 M $FeCl_3$ solution due to transitions between energy levels related to the d-orbitals of Fe^{3+} ions. The 0.005 M $FeCl_3$ spectra indicate its suitability as a catalyst for organic synthesis[22]. Different absorbance values are revealed when 0.005 M $FeCl_3$ is added to liquid POME compared to fresh liquid POME. This is

caused by the Fe^{2+}/Fe^{3+} ion-exchange mediator in fresh liquid POME which causes the absorbance value to be reduced and shifted. Such effect is most probably related to the decline in the concentration of active species which is able to absorb UV light. The exact electronic transitions are dependent on the organic compounds present in fresh liquid POME and may arise from the synthesis of new by-products[23].

The 0.005 M $FeCl_3$ solution displays dominant absorption peaks at 241 nm and 301 nm wavelengths, indicating a transition between energy levels related to the d-orbitals of Fe^{3+} ions. A ligand-to-metal charge transfer (LMCT) transition refers to the process in which an electron is elevated from a ligand orbital to an unoccupied d-orbital of the metal ion. The absorption in the UV region of fresh liquid POME and liquid POME+0.005 M $FeCl_3$ can be connected to electronic transitions occurring within the organic compounds found in the fresh liquid POME. These transitions might involve the movement of an electron from a bonding π orbital to an antibonding π* orbital (referred to as π to π* transitions), or the movement of non-bonding electrons in n orbitals to π* orbitals (referred to as n to π* transitions)[24].

The organic compounds with conjugated double bonds found in fresh liquid POME, allow them to absorb UV light and transit from π to π*. In this process, an electron in a bonding π orbital is promoted to a higher-energy antibonding π* orbital, typically leading to absorption in the UV-visible region. Molecules containing non-bonding electrons (n) have the ability to undergo n to π* transitions, where a non-bonding electron is promoted to an antibonding π* orbital. These transitions often need lower energy compared to π to π* transitions and are frequently seen in compounds containing functional groups like carbonyls or nitro groups[25].

3.4   ATR-FTIR analysis

The ATR-FTIR spectrum of solid $FeCl_3$, dried solid POME, and dried solid POME+$FeCl_3$ is shown in Fig. 3. The solid $FeCl_3$ spectrum displays pronounced peaks at 1,615 nm in particular. This indicates the existence of vibrational functional groups that are characteristic of solid $FeCl_3$. Unlike the dried solid POME, the dried solid POME+$FeCl_3$ spectrum demonstrates different peak intensities because of chemical changes during degradation with 0.005 M $FeCl_3$. The peak at 3,418 nm which corresponds to O-H bond stretching may weaken, suggesting variations in the interactions and concentrations of hydroxyl groups[26]. The dried solid POME spectrum displays clear and well-defined peaks at 3,418 nm and 2,928 nm in particular, which correspond to O-H and C-H stretching vibrations, respectively. These peaks characterized the organic compounds found in the composition of POME[27].

Table 3 reflects the presence and characteristics of peaks observed in Fig. 3. The changes in the chemical bonds and vibration types on fresh liquid POME and liquid POME+$FeCl_3$ were due to the degradation process.

Based on the data in Table 3, the wavelength corresponding to the O-H stretch is observed at 3,418 nm. The results reveal the existence of hydroxyl groups (O-H) in both the dried solid POME+0.005 M $FeCl_3$ and dried solid POME samples, unlike solid $FeCl_3$ which does not display this characteristic. The O-H stretching identified might be caused by the presence of alcohol, phenol, or water molecules in both samples, but not in solid $FeCl_3$. The absorption observed at a wavelength of 2,928 nm and the formation of C-H stretch region were indicatives of vibrations associated with C-H stretching. This confirms the existence of organic compounds that contain methyl or methylene functional groups but not in solid $FeCl_3$. This is due to the inorganic characteristic of $FeCl_3$ and non-existence of hydroxyl groups[28]. The presence of absorption at a wavelength of 2,358 nm was observed in the solid $FeCl_3$ sample, but it was not detected in either of the POME samples. Also, the specific type of bond associated with this absorption was not singled out. The absorption at 1,615 nm wavelength, which corresponds to the C=C/C=O stretching was associated with either the stretching vibrations of C=C bonds in aromatic compounds or the stretching of C=O bonds in carbonyl groups. The solid $FeCl_3$ prominently exhibits a visible peak at this specific wavelength, which may be attributed to the coordination of the ion Fe^{3+}. Both POME samples also display similar absorption, and it is suspected that the existence of unsaturated or carbonyl chemicals in both the dried solid POME+0.005 M $FeCl_3$ and dried solid POME samples[29] contributed to it.
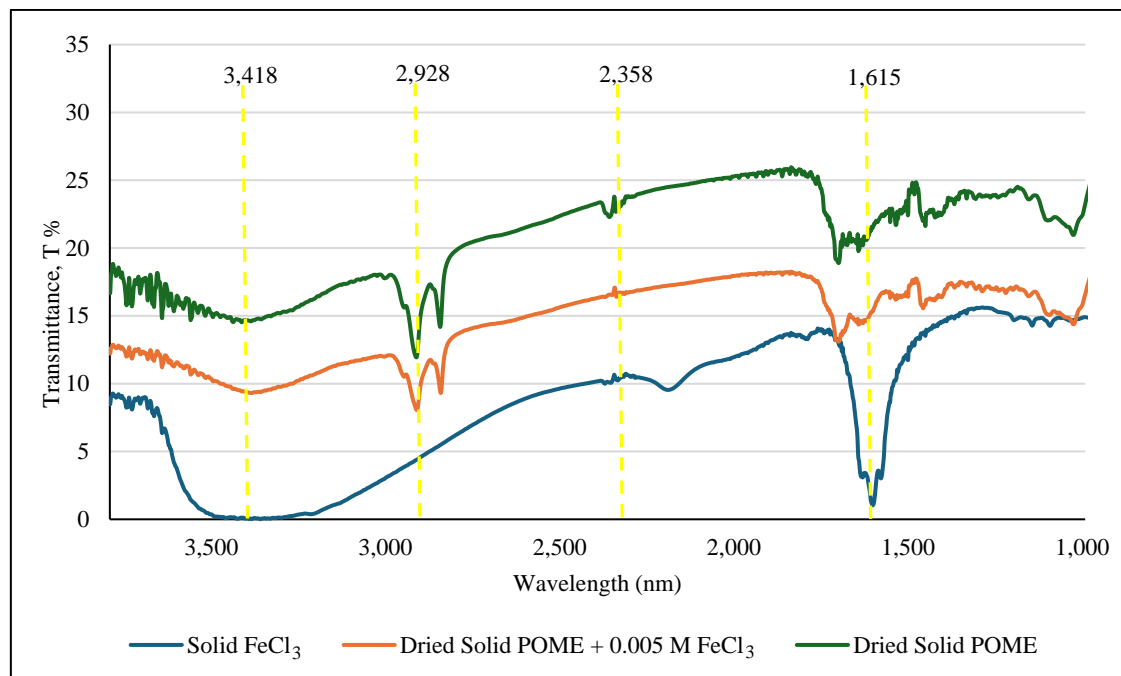
Fig. 3. FTIR Spectrum of dried solid POME, dried solid POME+0.005 M FeCl₃ and solid FeCl₃.

Table 3. FTIR spectrum analysis data and the possible bonding found

Sample	3,418 nm (O-H Stretch)	2,928 nm (C-H Stretch)	2,358 nm (C-H)	1,615 nm (C=C/C=O Stretch)
Solid of $FeCl_3$	Absent	Absent	Present	Present (Prominent)
Dried solid POME+$FeCl_3$	Present	Present	Absent	Present
Dried solid POME	Present	Present	Absent	Present

Overall, the analysis of the solid $FeCl_3$ sample shows the absence of absorption feature of organic compounds but the existence of a significant peak at 1,615 nm, revealing that it is primarily composed of inorganic components. The presence of O-H and C-H stretches in the dried solid POME+0.005 M $FeCl_3$ sample suggests that the degradation process with 0.005 M $FeCl_3$ failed to eliminate these functional groups completely. This analysis reveals a diverse composition of organic compounds present in both dried solid POME and dried solid POME+$FeCl_3$.

3.5   XRD analysis

XRD is a scientific method employed to ascertain the crystallographic arrangement, crystalline phase, and further structural characteristics of materials. The peak which exhibits the greatest intensity is the most dominant crystallographic plane present in the sample. In Fig. 4, the XRD pattern shows peaks at different 2θ angles, corresponding to different crystallographic planes of the compound. The peaks are labelled with their respective Miller indices. The highest crystallinity characteristics are displayed by a principal peak at peak (c). The sharp peaks revealed in the XRD diffractogram authenticate the presence of crystalline properties. Every peak corresponds to a set of crystallographic planes that reflect X-rays at specific angles according to Bragg's law. The primary peak indicates a well-organised structure with a

prevailing alignment of crystals. A reference pattern from the Joint Committee on Powder Diffraction Standards (JCPDS) file number 19-0629 for comparison is also included in the graph. This database provides standard reference patterns for material identification and crystallographic analysis. The XRD pattern of $FeCl_3.6H_2O$ exhibits distinct peaks and confirms the crystalline nature of the material.
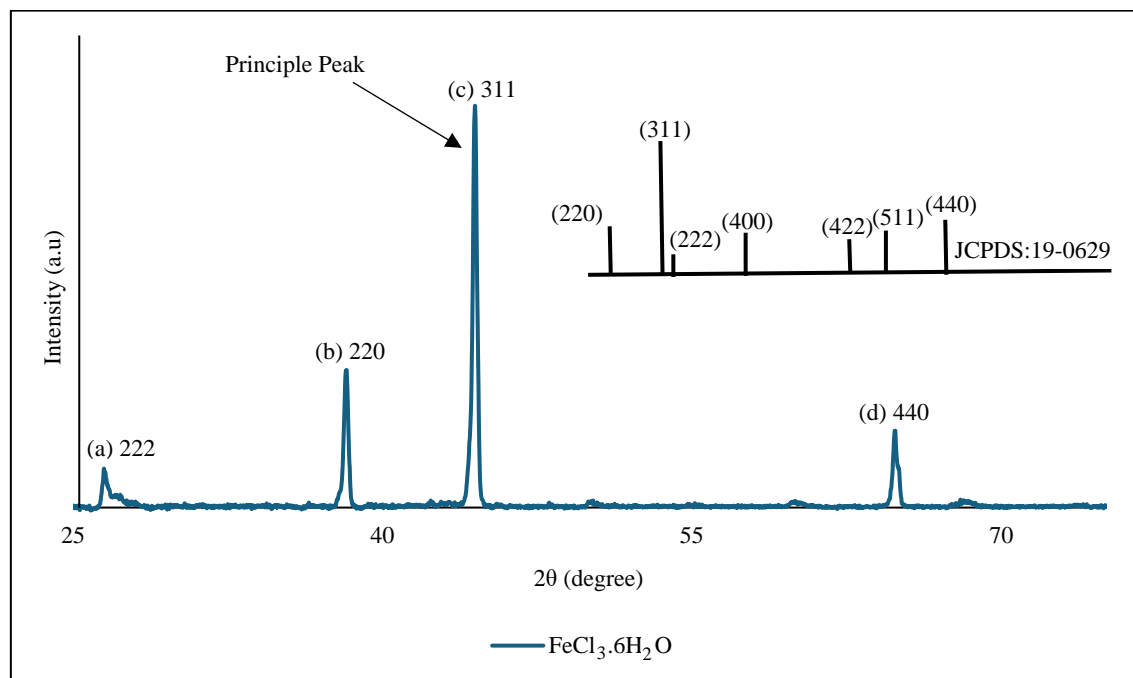
Fig. 4. XRD diffractogram of solid $FeCl_3 \cdot 6H_2O$ with JCPDS No. 19-0629.

Table 4 shows the information regarding the peaks pattern of $FeCl_3 \cdot 6H_2O$ with JCPDS No. 19-0629[30]. It shows the principal peak (c) at 2θ range 45–55 degrees, with Miller indices (311), as the most intense peak. This is mainly attributed to the primary crystallographic orientation and thus, confirms the presence of the 311 plane in the crystal lattice. As for the secondary peaks, they are labelled as follows: (a) 222 at a range of 30–35 degrees, (b) 220 at a range of 35–45 degrees, and (d) 440 at a range of 68–75 degrees. Peak (a), corresponds to the 222 plane, is less intense than other secondary peaks. While peak (d) corresponds to the 440 plane in the range of 68–75 degrees, completes the identification of significant crystallographic reflections. The observed peaks were confirmed to match the JCPDS reference pattern.

Table 4. Peaks pattern of $FeCl_3 \cdot 6H_2O$ with JCPDS No. 19-0629

Peak Label	2θ (degree)	Miller indices	Description
a	30-35	(222)	Secondary Peak
b	35-45	(220)	Secondary Peak
c	45-55	(311)	Principal Peak
d	68-75	(440)	Secondary Peak
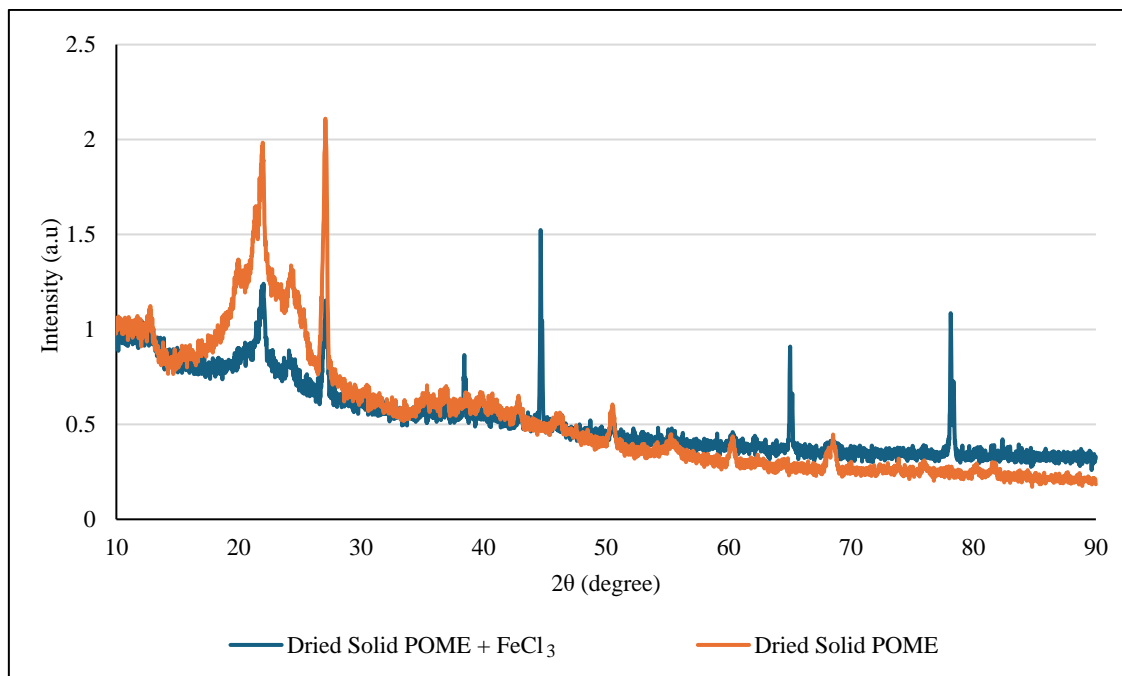
Fig. 5. XRD diffractograms of dried solid and dried solid POME+FeCl₃.

   Fig. 5 shows two X-ray diffraction (XRD) patterns employed for the identification of the crystalline structure of materials. The XRD diffractogram exhibits distinct peaks that correspond to the scattering of X-rays from the atomic planes within the crystal lattice of the samples. The two diffractograms represent dried solid POME+FeCl$_3$ and dried solid POME. The presence of sharp peaks indicates the presence of crystalline materials, and the height of each peak corresponds to a specific crystalline phase[31]. Both dried solid POME+FeCl$_3$ and dried solid POME display distinct peak characteristics in XRD patterns and variations in the intensity and the number of peaks were also observed. The dried solid POME exhibits a distinct peak at a lower 2θ (degree) value, but such a distinct peak is absent in the dried solid POME+FeCl$_3$. This indicates a variation in the crystalline composition between the two samples. The dried solid POME+FeCl$_3$ displays multiple distinct peaks that are less prevalent compared to those in the dried solid POME. These differences most likely are the result of changes in the crystalline phases of POME, which occurred during the adding of catalyst (0.005 M FeCl$_3$) in the degradation process. Thus, the dried solid POME+FeCl$_3$ exhibits an increased background intensity compared to the dried solid POME. This suggests that the dried solid of POME+FeCl$_3$ sample contains an amorphous component that contributes to the diffuse scattering observed in the background. Despite the presence of sharp peaks indicating crystalline phases, the overall increase in background intensity points to the coexistence of amorphous material within the sample. The dual presence of crystalline and amorphous phases was due to the chemical changes and interactions introduced by the addition of FeCl$_3$ during the degradation process[32].

3.6 BET analysis

   Table 5 shows the results obtained from a Brunauer-Emmett-Teller (BET) analysis of dried solid POME and dried solid POME+FeCl$_3$. BET analysis is a technique employed to quantify the precise surface area of materials, usually by measuring the absorption of gas onto the surface of the material. Surface area (m² g^{-1}) refers the total area per unit mass of a sample[33]. The dried solid POME has a surface area of 0.94 m² g^{-1}, but the dried solid POME+FeCl$_3$ exhibits a substantially larger surface area of 18.55 m² g^{-1}. The adsorption size (nm) is the mean pore diameter on the material's surface which is determined through

adsorption measurements. The dried solid POME has an adsorption size of 10.49 nm, while the dried solid POME+FeCl$_3$ has a greater adsorption size of 21.88 nm.

Table 5. BET Analysis of dried solid POME and dried solid POME+FeCl$_3$

Parameter	Dried solid POME	Dried solid POME+FeCl$_3$	Percentage %
Surface Area (m^2 g^{-1})	0.94	18.55	94.82
Adsorption, nm	10.49	21.88	52.07
Desorption, nm	31.59	18.41	3.17

The surface area of dried solid POME+FeCl$_3$ increased substantially from 0.94 m² g^{-1} to 18.55 m² g^{-1} compared to dried solid POME, reflecting a 94.82% increase. This notable change in porosity enhances its reactivity, specifically in adsorption capacity. The adsorption capacity of dried solid POME+FeCl$_3$ increased by 52.07%, from 10.49 nm to 21.88 nm compared to dried solid POME. This is due to the addition of catalyst (0.005 M FeCl$_3$) which modified the surface area during the chemical synthesis reaction. The desorption capacity of dried solid POME decreased slightly by 3.17%, from 31.59 nm to 18.41nm when compared to dried solid POME+FeCl$_3$. This implies a stronger binding of substances in dried solid POME+FeCl$_3$ compared to dried solid POME.

The observed increase in surface area from dried solid POME to dried solid POME+FeCl$_3$ indicates that the process of degradation in liquid POME has considerably changed the material's properties which potentially leads to an increase in porosity and surface roughness. The difference in the adsorption and desorption diameters indicates distinct pore architectures between dried solid POME and dried solid POME+FeCl$_3$. The changes in the desorption size of dried solid POME reveal that the material has an intricate pore structure, and there is a possibility that the pores of different sizes become inaccessible during the desorption process. The BET analysis has revealed both dried solid POME and dried solid POME+FeCl$_3$ have mesoporous characteristics[34]. Thus, the reduction in desorption size for the dried solid POME+FeCl$_3$ compared to its adsorption size is unforeseen and may be due to pore blockage that hinders the accessibility of pores during desorption.

4   CONCLUSION

Overall, the utilisation of Fe^{2+}/Fe^{3+} ion exchange mediator as a mediator for POME degradation through synthesis reaction shows significant potential for improving the sustainability of palm oil production by enabling more efficient biomass treatment like POME. The study establishes a basis for further investigation and advancement of more effective POME treatment techniques which could result in decreased ecological consequences.

CONFLICT OF INTEREST

The authors declare that they have no known competing financial interests or personal relationships that could have appeared to influence the work reported in this paper.

AUTHORS' CONTRIBUTIONS

Conceptualisation: M. H. Md Ali
Data curation: M. H. Md Ali
Methodology: M. H. Md Ali
Formal analysis: M. H. Md Ali
Visualisation: Z. Mohd Zain
Software: H. Mohd Zaki
Writing (original draft): M. H. Md Ali
Writing (review and editing): M. A. Mohd Fauzi
Validation: C. C. Tay
Supervision: M. Noor Jalil
Funding acquisition: Not applicable
Project administration: M. Noor Jalil

REFERENCES

1. Nasrin, A. B., Raman, A. A. A., Sukiran, M. A., Bukhari, N. A., Buthiyappan, A., Subramaniam, V., Aziz, A. A., & Loh, S. K. (2023). Renewable energy and greenhouse gases emission reduction potential of biogas from palm oil mill effluent. *Journal of Oil Palm Research*, *36*(2)*,* 456–468. https://doi.org/10.21894/jopr.2023.0032

2. Al-Amshawee, S. K., Yunus, M. Y., & Azoddein, A. A. (2020). A review on aerobic biological processes for palm oil mill effluent: Possible approaches. *IOP Conference Series: Materials Science and Engineering*, *736*(2), 022035. https://doi.org/10.1088/1757-899X/736/2/022035

3. Awere, E., Bonoli, A., & Obeng, P. A. (2021, April). Correction to: Characterization of palm oil mill wastewater: The case of small-scale mills in Ghana. In J. N. Mojekwu, W. Thwala, C. Aigbavboa, L. Atepor, & S. Sackey (Eds.), *Sustainable Education and Development* (pp. 335–334). Springer. https://doi.org/10.1007/978-3-030-68836-3_29

4. Mohammad, S., Baidurah, S., Kobayashi, T., Ismail, N., & Leh, C. P. (2021). Palm oil mill effluent treatment processes-A review. *Processes*, *9*(5), 1–22. https://doi.org/10.3390/pr9050739

5. Chang, X., Zhang, X., & Chen, Z. (2018). $FeCl_3$ or $MeSO_3H$-promoted multicomponent reactions for facile synthesis of structurally diverse furan analogues. *Organic & Biomolecular Chemistry*, *16*(23), 4279–4287. https://doi.org/10.1039/c8ob00942b

6. Sahoo, R. K., Rana, G., Kar, A., Ghosh, S., & Jana, U. (2024). Iron(III)-catalysed povarov cyclisation for the synthesis of fused dibenzo[b,f][1,7]naphthyridine embedded arylpyrrolo scaffolds. *Synthesis*, *57*(01), 147–153. https://doi.org/10.1055/a-2349-6836

7. Zhou, N., Zhang, C., Cao, Y., Zhan, J., Fan, J., Clark, J. H., & Zhang, S. (2021). Conversion of xylose into furfural over MC-SnOx and NaCl catalysts in a biphasic system. *Journal of Cleaner Production, 311,* 127780. https://doi.org/10.1016/j.jclepro.2021.127780

8. Abeish, A. M., Ang, H. M., & Znad, H. (2015). Role of ferric and ferrous ions in the enhancement of the heterogeneous solar photocatalytic degradation of combined mixture of chlorophenols. *Water Science and Technology*, *72*(9), 1561–1568. https://doi.org/10.2166/wst.2015.374

9. Chávez Rivas, F., Rodríguez-Iznaga, I., Berlier, G., Tito Ferro, D., Concepción-Rosabal, B., & Petranovskii, V. (2019). Fe speciation in iron modified natural zeolites as sustainable environmental catalysts. *Catalysts*, *9*(10), 866. https://doi.org/10.3390/catal9100866

10. McGrath, M. J., Patterson, N., Manubay, B. C., Hardy, S. H., Malecha, J. J., Shi, Z., Yue, X., Xing, X., Funke, H. H., Gin, D. L., Liu, P., & Noble, R. D. (2019). 110th anniversary: The dehydration and loss of ionic conductivity in anion exchange membranes due to $FeCl_4^-$ ion exchange and the role of membrane microstructure. *Industrial & Engineering Chemistry Research*, *58*(49), 22250–22259. https://doi.org/10.1021/acs.iecr.9b04592

11. Gérard, V., Ay, E., Launay, V., Galopin, C., Morlet-Savary, F., & Lalevée, J. (2022). Improvement of color stability using a chelating agent in model soft beverages subjected to Fenton reaction. *Journal of the Chinese Chemical Society*, *69*(7), 1096–1105. https://doi.org/10.1002/jccs.202200164

12. Shen, J., Liang, J., Fu, X., Jiang Y., Yan, S., He, H., & Ren, X. (2020). Facile synthesis of CuMgFe layered double hydroxides for efficient catalytic phenol hydroxylation under mild conditions. *ChemistrySelect*, *5*(9), 2835–2841. https://doi.org/10.1002/slct.201904242

13. Pang, Y., & Bjornsson, R. (2023). Understanding the electronic structure basis for N_2 binding to FeMoco: A systematic quantum mechanics/molecular mechanics investigation. *Inorganic Chemistry*, *62*(14), 5357–5375. https://doi.org/10.1021/acs.inorgchem.2c03967

14. Chen, Z. (2024). Application of UV-vis spectroscopy in the detection and analysis of substances. *Transactions on Materials, Biotechnology and Life Sciences*, *3*, 131–136. https://doi.org/10.62051/mw4daz69

15. Wei, C. C., Lin, P. H., Hsu, C. E., Jian, W. B., Lin, Y. L., Chen, J. T., Banerjee, S., Chu, C. W., Khedulkar, A. P., Doong, R. A., & Tsukagoshi, K. (2024). Boosting areal capacitance in WO_3-based supercapacitor materials by stacking nanoporous composite films. *Cell Reports Physical Science*, *5*(3), 101836. https://doi.org/10.1016/j.xcrp.2024.101836

16. Dutta, A., Mishra, D. K., Kundu, D., Mahanta, U., Jiang, S. P., Silvester, D. S., & Banerjee, T. (2022). Examining the electrochemical nature of an ionogel based on the ionic liquid $[P_{66614}][TFSI]$ and TiO_2: Synthesis, characterization, and quantum chemical calculations. *Industrial & Engineering Chemistry Research*, *61*(25), 8763–8774. https://doi.org/10.1021/acs.iecr.2c00550

17. Suen, J. W., Elumalai, N. K., Debnath, S., Mubarak, N. M., Lim, C. I., Mohan, R. M., & Khalid, M. (2023). Study of capacitive behavior and its inter-relationship with electrolyte solution concentration in hybrid ionogels. *ECS Journal of Solid State Science and Technology*, *12*(9), 097001. https://doi.org/10.1149/2162-8777/acf2c3

18. Hussein, S. Q., Gomaa, E. A., El-Defrawy, M. M., El-Ghalban, M. G., & AbouElleef, E. M. (2024). Study of the electrochemical properties of iron ions in various solutions including human blood using glassy carbon electrode and some theoretical applications. *Journal of Molecular Liquids*, *408*, 125366. https://doi.org/10.1016/j.molliq.2024.125366

19. Hamzah, N. A., Md Sahar, M. A. A. Z., Tan, A. K., Ahmad, M. A., Abdul Malik, M. F. I., Loo, C. C., Chang, W. S., & Ng, S. S. (2023). Effects of indium composition on the surface morphological and optical properties of InGaN/GaN heterostructures. *Microelectronics International*, *40*(1), 8–16. https://doi.org/10.1108/mi-03-2022-0042

20. Aldabib, J. M., & Edbeib, M. F. (2020). The effects of concentration based on the absorbance form the ultraviolet–visible (UV-VIS) spectroscopy analysis. *International Journal of Science Letters*, *2*(1), 1–11. https://doi.org/10.38058/ijsl.633876

21. Meng, R., Su, H., Zhu, S., Pan, Y., Pan, R., Liu, R., & Zhu, H. (2022). Synthesis, spectroscopic characteristics, DFT study and dyeing performance of bischlorotriazine based water-soluble reactive dyes. *ChemistrySelect, 7*(20), e202200993. https://doi.org/10.1002/slct.202200993

22. Wang, X., Shi, C., Yang, M., Ma, Y., Chen, Y., Tang, W., Lü, T., & Feng, J. (2023). Photoredox synthesis of Vicinal Dichloride using $FeCl_3$ as chlorine source. *Asian Journal of Organic Chemistry, 12*(6), e202300077. https://doi.org/10.1002/ajoc.202300077

23. Persson, I. (2018). Ferric chloride complexes in aqueous solution: An EXAFS study. *Journal of Solution Chemistry, 47,* 797–805. https://doi.org/10.1007/s10953-018-0756-6

24. Hirschhausen, T., Fritsch, L., Lux, F., Steube, J., Schoch, R., Neuba, A., Egold, H., & Bauer, M. (2023). Iron(III)-complexes with *N*-phenylpyrazole-based ligands. *Inorganics, 11*(7), 282. https://doi.org/10.3390/inorganics11070282

25. Kuball, H. G., Höfer, T., & Kiesewalter, S. (2017). Chiroptical spectroscopy, general theory. In J. C. Lindon, G. E. Tranter, D. W. Koppenaal (Eds.), *Encyclopedia of spectroscopy and spectrometry* (3rd ed., pp. 217–231). Academic Press. https://doi.org/10.1016/B978-0-12-409547-2.04980-5

26. El Yakoubi, N., Ennami, M., El Ansari, Z. N., Ait Lhaj, F., Bounab, L., El Kbiach, M., & El Bouzdoudi, B. (2023). Utilization of Ziziphus lotus fruit as a potential biosorbent for lead (II) and cadmium (II) ion removal from aqueous solution. *Ecological Engineering & Environmental Technology, 24*(3), 135–146. https://doi.org/10.12912/27197050/159631

27. Dwiwibangga, Y., Safitri, A., & Fatchiyah, F. (2022). Profiling of phytochemical compounds of East Java Red Rice Bran has the high-value biological activities as antioxidant and antidiabetic. *Indonesian Journal of Chemistry*, *22*(5), 1304–1320. https://doi.org/10.22146/ijc.73432

28. Kharat, P. B., Somvanshi, S. B., Khirade, P. P., & Jadhav, K. M. (2020). Induction heating analysis of surface-functionalized nanoscale $CoFe_2O_4$ for magnetic fluid hyperthermia toward noninvasive cancer treatment. *ACS Omega, 5*(36), 23378–23384. https://doi.org/10.1021/acsomega.0c03332

29. Setyawan, D., Permata, S. A., Zainul, A., & Lestari, M. L. A. D. (2018). Improvement in vitro dissolution rate of quercetin using cocrystallization of quercetin-malonic acid. *Indonesian Journal of Chemistry, 18*(3), 531–536. https://doi.org/10.22146/ijc.28511

30. Harris, R. A. (2023). Simulation and experimental study of cuboid and spherical magnetic Fe_3O_4 nanoparticles prepared with NaOH and NH_4OH. *Applied Physics A*, *129*(12), 851. https://doi.org/10.1007/s00339-023-07128-5

31. Raja, T., Yuvarajan, D., Ali, S., Dhanraj, G., & Kaliappan, N. (2024). Fabrication of glass/madar fibers reinforced hybrid epoxy composite: A comprehensive study on the material stability. *Scientific Reports, 14,* 8374. https://doi.org/10.1038/s41598-024-53178-x

32. Booysen, T. N., Jamiru, T., Adegbola, T., & Arthur, N. (2023). Microstructural effects on properties of as-fabricated inconel 625 with direct energy deposition process. *MATEC Web of Conferences*, *388*, 08001. https://doi.org/10.1051/matecconf/202338808001

33. Kwiatkowski, M., & Broniek, E. (2021). Computer analysis of the porous structure of activated carbons derived from various biomass materials by chemical activation. *Materials*, *14*(15), 4121. https://doi.org/10.3390/ma14154121

34. Saheed, I. O., Oh, W. D., Latip, A. F. A., & Suah, F. B. M. (2022). Mesoporous chitosan/activated charcoal powder and bead modified in 1-butyl-3-methylimidazolium acetate for the adsorption of acid blue 25 from an aqueous solution. *Journal of Chemical Technology & Biotechnology*, *97*(5), 1315–1325. https://doi.org/10.1002/jctb.7027